



Cite this: DOI: 10.1039/d2cp04042e

A penta-silicene nanoribbon-based 3D silicon allotrope with high carrier mobility and thermoelectric performance†

 Yiheng Shen, Dongyuan Ni, Yanyan Chen, Jie Sun and Qian Wang *

Motivated by the successful synthesis of penta-silicene nanoribbons using various experimental techniques, we design a new 3D silicon allotrope, labeled cco-Si₄₈, by assembling such nanoribbons, confirm its dynamical, thermal and mechanical stabilities, and further study its electron/phonon transport and linear optical properties based on the state-of-the-art theoretical calculations. We find that cco-Si₄₈ is a direct bandgap semiconductor with a gap of 1.46 eV, exhibiting a high hole mobility in the magnitude of 10³ cm² V⁻¹ s⁻¹ and a low lattice thermal conductivity of 6.33 W m⁻¹ K⁻¹ at 300 K. Unlike the commonly reported n-type silicon-based materials with high thermoelectric performance, the p-type cco-Si₄₈ outperforms its n-type counterpart in the thermoelectric figure of merit (*ZT*) value with a considerable value of 0.57 at 800 K. We further demonstrate that the electron–phonon interactions play a critical role in determining the optimal carrier concentrations for the peak *ZT* values. This work expands penta-silicene nanoribbons to their 3D assembled structure with new features and applications.

 Received 31st August 2022,
 Accepted 19th October 2022

DOI: 10.1039/d2cp04042e

rsc.li/pccp

1. Introduction

Rational design and synthesis of new silicon materials are of great interest because of their compatibility with the well-developed silicon-based semiconductor industry. Penta-silicene nanoribbons (PSNRs) are such an example, and have been extensively studied experimentally and theoretically motivated by the theoretical prediction of penta-graphene.^{1,2} For instance, in 2016, Jorge *et al.*³ reported the pentagonal nature of perfectly aligned single and double-strand Si-nanoribbons grown on the Ag(110) surface. Later on, Geoffroy *et al.*⁴ carried out systematic studies to further validate the pentamer model of silicene grown on a reconstructed surface by grazing-incidence X-ray diffraction and scanning tunneling microscopy. In 2018, Sheng *et al.*⁵ studied penta-Si nanoribbons grown on Ag(110) by using non-contact atomic force microscopy and tip-enhanced Raman spectroscopy. Yue *et al.*⁶ observed one-dimensional (1D) topological electronic states in PSNRs. Furthermore, based on the research progress in 1D PSNRs, Guo *et al.*⁷ carried out the first study on a stable 2D tilted penta-Si sheet, which exhibits in-plane ferroelectricity with a Curie temperature of 1190 K. Recently, Zhan *et al.*⁸ designed a

semimetallic 2D tilted penta-Si sheet with distorted Dirac cones in the absence of spin–orbit coupling (SOC). When SOC is considered, it becomes a topological insulator with helical edge states and a gap opening of 2.4 meV at the Dirac point. These studies show that pentagon-based silicon nanostructures have received considerable attention. Because significant progress has been made in the synthesis of 3D porous carbon materials by using graphene nanoribbons as the building blocks for multiple applications,^{9,10} it is highly desirable to explore the possibility of design and synthesis of stable 3D penta-Si allotropes by assembling penta-silicene nanoribbons.

Meanwhile, in addition to the conventional applications of silicon-based materials in photovoltaics, the thermoelectric performances of these materials have been extensively studied in recent years, which are evaluated by a dimensionless figure of merit $ZT = S^2\sigma T/(\kappa_e + \kappa_L)$, where a high *ZT* value indicates a high thermoelectric efficiency. Here, *S*, σ , κ_e , and κ_L are the Seebeck coefficient, electrical conductivity, electronic thermal conductivity, and lattice thermal conductivity, respectively. Despite the fact that diamond silicon is inappropriate for such applications due to its high thermal conductivity (~ 150 W m⁻¹ K⁻¹),¹¹ nanostructured bulk silicon¹² and silicon nanowires¹³ have been developed as efficient thermoelectric materials with enhanced *ZT* values (0.7 at over 1200 K and 0.6 at room temperature, respectively) due to their inherited high carrier mobilities and reduced thermal conductivities. In addition, the thermoelectric properties of several other metastable

CAPT, School of Materials Science and Engineering, BKL-MEMD, Peking University, Beijing 100871, China. E-mail: qianwang2@pku.edu.cn

† Electronic supplementary information (ESI) available. See DOI: <https://doi.org/10.1039/d2cp04042e>

silicon allotropes, like BC8 silicon¹⁴ and clathrate Si₁₃₆,¹⁵ are also promising, because their complex geometries lead to decreased lattice thermal conductivities.¹⁶ Thus, it is intuitive to expect a good thermoelectric performance of the PSNR-based 3D silicon allotrope.

In this study, we rationally design a 3D silicon allotrope termed cco-Si₄₈ based on the PSNR building blocks. We confirm that it is a thermally, dynamically and mechanically stable semiconductor with a direct bandgap. We perform electron transport property calculations by considering *ab initio* electron–phonon (e–ph) interactions, calculate the lattice thermal conductivity at the three-phonon scattering level, and evaluate its potential for thermoelectric applications. We further demonstrate the necessity to include e–ph interactions when calculating thermoelectric performances at ambient and high temperatures.

2. Computational methods

Our first-principles density functional theory calculations are performed using the Vienna *ab initio* simulation package (VASP)^{17,18} and Quantum ESPRESSO (QE) package.^{19,20} Geometry optimization and electronic structure calculations are performed using the VASP, where the interactions between ion cores and valence electrons are treated with the projected augmented wave method.²¹ The plane waves with a kinetic energy cutoff of 600 eV are used to expand the wave functions of these electrons. The exchange–correlation interaction among the valence electrons is treated by the Perdew–Burke–Ernzerhof (PBE) functional²² within the scheme of generalized gradient approximation (GGA)²³ for geometry optimization and some property calculations and by the Heyd–Scuseria–Ernzerhof (HSE06) hybrid functional^{24,25} for the electronic structure calculations. A $9 \times 9 \times 5$ \mathbf{k} mesh is used in these calculations for the integration over the first Brillouin zone. The thresholds for the convergence of total energy and interatomic forces are 10^{-8} eV and 10^{-6} eV Å⁻¹, respectively. The Nosé–Hoover thermostat²⁶ is used to control the temperature fluctuation in the *ab initio* molecular dynamic (AIMD) simulations under the canonical ensemble in the VASP.

For calculating the e–ph interactions, the ground-state electronic structure is calculated at the GGA-PBE level by QE using the norm-conserving pseudopotentials from PseudoDojo,²⁷ a kinetic energy cutoff of 60 Ry, a $6 \times 6 \times 4$ \mathbf{k} mesh, and an energy convergence threshold of 10^{-15} Ry. It is then transformed into the maximally localized Wannier representation^{28,29} with the WANNIER90 program.³⁰ Density functional perturbation theory calculations are carried out using QE to obtain the dynamic matrix at a $3 \times 3 \times 2$ \mathbf{q} mesh. The e–ph matrix elements $g_{mn\nu}(\mathbf{k}, \mathbf{q})$ are calculated on the coarse \mathbf{k} and \mathbf{q} meshes and interpolated on a finer $24 \times 24 \times 12$ grid using the Perturbo code³¹ with the following equation:

$$g_{mn\nu}(\mathbf{k}, \mathbf{q}) = \sqrt{\frac{\hbar}{4\pi\omega_{\nu\mathbf{q}}}} \sum_{\lambda z} \frac{e^{\lambda z}}{\sqrt{M_{\lambda}}} \langle \psi_{m\mathbf{k}+\mathbf{q}} | \partial_{\mathbf{q},\lambda z} V | \psi_{n\mathbf{k}} \rangle \quad (1)$$

where M_{λ} is the atomic mass of atom λ , $|\psi_{m\mathbf{k}+\mathbf{q}}\rangle$ and $|\psi_{n\mathbf{k}}\rangle$ are the wave functions of the two electronic states coupled by the phonon mode $\nu\mathbf{q}$ with the frequency $\omega_{\nu\mathbf{q}}$, $\mathbf{e}_{\nu\mathbf{q}}^{\lambda z}$ is the eigenvector of the phonon mode $\nu\mathbf{q}$ projected on atom λ and the Cartesian direction z , and $\partial_{\mathbf{q},\lambda z} V$ is the corresponding perturbation potential. The mode-resolved electron relaxation time is deduced from the interpolated e–ph matrix with an iterative solution of the linearized electron Boltzmann transport equation (BTE),³² from which the transport properties of charge carriers are calculated in Perturbo, including carrier mobility μ , electrical conductivity σ , Seebeck coefficient S , and electronic thermal conductivity κ_e .³³

For calculating the intrinsic lattice thermal conductivity κ_L , an iterative solution of the linearized phonon BTE³⁴ is used as implemented in the ShengBTE code.³⁵ The solution to the BTE is applied to the following equation for κ_L values:

$$\kappa_L^{\alpha\beta} = \frac{1}{k_B T^2 \Omega N} \sum_{\nu\mathbf{q}} f_{0,\nu\mathbf{q}}^{\text{BE}} (f_{0,\nu\mathbf{q}}^{\text{BE}} + 1) \left(\frac{\hbar c_{\nu\mathbf{q}}}{2\pi} \right)^2 v_{\nu\mathbf{q}}^{\alpha} F_{\nu\mathbf{q}}^{\beta} \quad (2)$$

where α/β denotes the Cartesian direction $x/y/z$, Ω is the volume of the primitive cell, N is the number of uniform \mathbf{q} points, and $f_{0,\nu\mathbf{q}}^{\text{BE}}$, $v_{\nu\mathbf{q}}^{\alpha}$ and $F_{\nu\mathbf{q}}^{\beta}$ are the equilibrium Bose–Einstein distribution, the group velocity and the mean free path of the phonon mode $\nu\mathbf{q}$, respectively. The BTE is solved on a $15 \times 15 \times 7$ \mathbf{q} -mesh based on the 2nd-order and 3rd-order interatomic force constants (IFCs). The 2nd-order IFCs are calculated by using the finite displacement method³⁶ as implemented in the Phonopy package,³⁷ and the 3rd-order IFCs are obtained by least-square fitting from the interatomic forces in 300 randomly displaced $3 \times 3 \times 1$ supercells of cco-Si₄₈ using the HiPhive package.³⁸ During the fitting process, 1% of the raw data is used as the test set. The cutoff radius for the 3rd-order IFCs, the ratio between the target IFC values and the raw interatomic force data and the goodness of fit values in the training and test sets are 6.0 Å, $\sim 1:9$, 0.99987, and 0.99983, respectively.

3. Results and discussion

3.1. Geometry and stability

Si atoms tend to form sp³-like hybridizations because the 3p_z–3p_z π bond between the adjacent Si atoms is weak. In the case of three-fold coordinated Si atoms, they tend to form a tilted geometry so that the electrons can congregate on one Si atom and lower the energy, as is the case with penta-silicene.⁷ To this end, we align the PSNRs along the y direction and stack them up along the x direction. After geometry optimization, the Si atoms in the PSNRs are distorted from the planar configuration, as shown in Fig. 1(a), so that each of the three- and two-fold coordinated Si atoms in the PSNR can form an extra chemical bond with an atom from the neighboring PSNRs at the x and z directions, respectively, leading to a periodic unit cell with a c-centered orthorhombic $Cmca$ symmetry (space group no. 64) that contains 48 Si atoms. Hence, we refer to it as cco-Si₄₈. Detailed information about the construction process can be found in Text S1 and Fig. S1 in the ESI.† The lattice parameters are $a = 6.45$ Å, $b = 11.43$ Å and $c = 14.14$ Å. In this

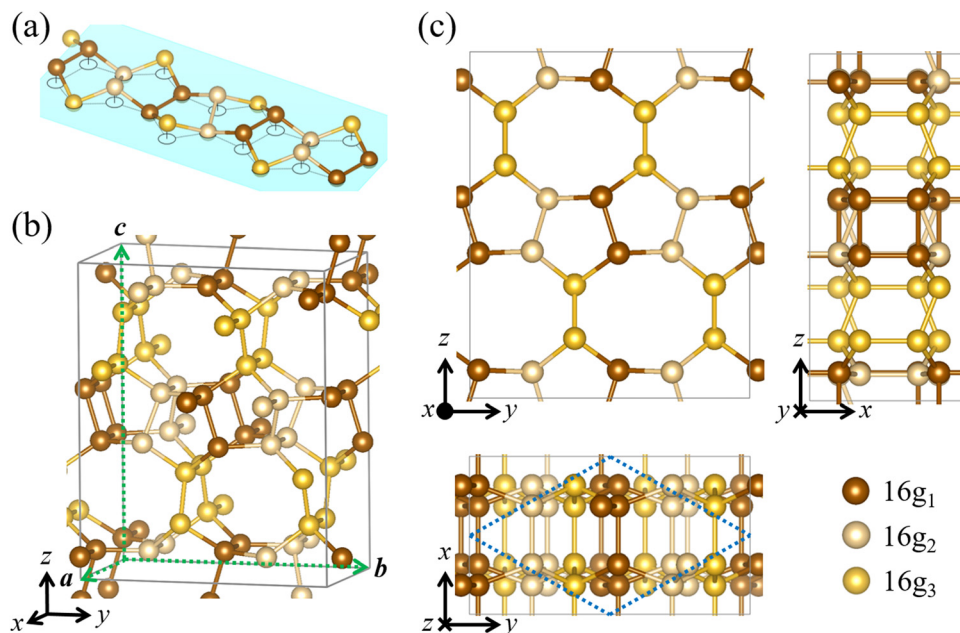


Fig. 1 (a) Schematic of the PSNR building block. The silicon atoms are either on or above the cyan plane. (b) Perspective view of the cco-Si_{48} unit cell. The green arrows denote the lattice vectors. (c) Optimized unit cell of cco-Si_{48} . The blue dashed rhombus illustrates the shape of the primitive cell.

structure, the 48 Si atoms occupy three nonequivalent Wyckoff positions, namely, $16g_1$ (0.315, 0.531, 0.919), $16g_2$ (0.185, 0.723, 0.924) and $16g_3$ (0.184, 0.374, 0.828), which are represented by the brown, pale gold and yellow spheres, respectively, as shown in Fig. 1(b) and (c). The atoms at the $16g_1$ and $16g_2$ sites are four-fold coordinated, forming Si_4 rings and armchair-like Si chains that connect the stacked PSNRs along the x direction, respectively, while the atoms at the $16g_3$ site are three-fold coordinated, forming tilted Si_2 dimmers and connect the adjacent PSNRs along the z direction in a head-on pattern. To check the experimental feasibility of this new silicon allotrope, we compare its formation energy E_{form} with that of other synthesized silicon allotropes, which is defined as $E_{\text{form}} = E(\text{silicon allotrope}) - E(\text{diamond silicon})$, where $E(X)$ is the total energy of the silicon allotrope X on a per atom basis. The cco-Si_{48} structure possesses a low E_{form} value of

0.08 eV per atom, which is lower than those of many synthesized silicon allotropes including BC8 silicon (0.16 eV per atom) and R8 silicon (0.16 eV per atom) while larger than that of hexagonal diamond silicon (0.01 eV per atom). Together with its bottom-up design, the energetically low-lying feature of cco-Si_{48} indicates that it could be stabilized.

We first confirm the dynamical stability of cco-Si_{48} by calculating its phonon band structure. For displaying the phonon band dispersion, the following high-symmetry path $\text{T}(-0.5, -0.5, 0.5) \rightarrow \text{Z}(0.0, 0.0, 0.5) \rightarrow \text{R}(0.0, -0.5, 0.5) \rightarrow \text{S}(0.0, -0.5, 0.0) \rightarrow \Gamma(0.0, 0.0, 0.0) \rightarrow \text{Y}(-0.5, -0.5, 0.0) \rightarrow \text{X}_1(-0.33, -0.67, 0.0) | \text{X}(0.33, -0.33, 0.0) \rightarrow \Gamma \rightarrow \text{Z} \rightarrow \text{A}(0.33, -0.33, 0.5) | \text{A}_1(-0.33, -0.67, 0.5) \rightarrow \text{T} \rightarrow \text{Y}$ is used, as illustrated in Fig. 2(a). The resulting phonon band structure in Fig. 2(b) has no any imaginary phonon modes, indicating that cco-Si_{48} is dynamically stable.

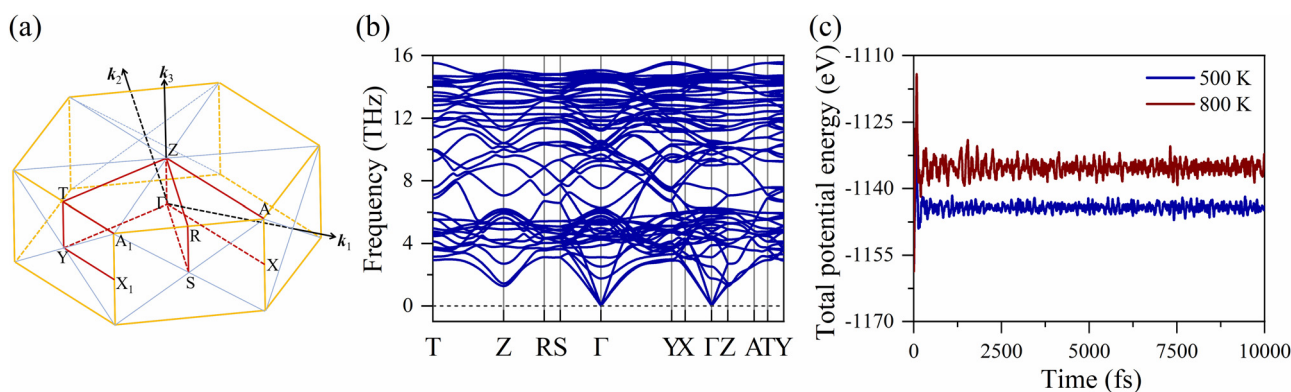


Fig. 2 (a) High symmetry path in the first Brillouin zone and (b) phonon band structure of cco-Si_{48} . (c) Fluctuation of total potential energy of cco-Si_{48} during AIMD simulations.

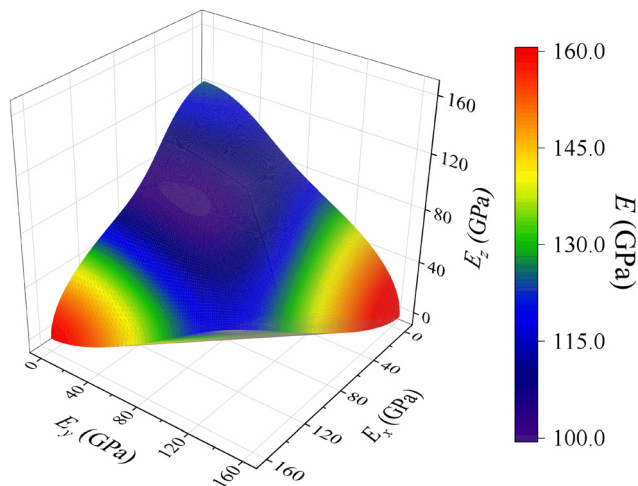


Fig. 3 Direction-dependence of Young's modulus E in cco-Si₄₈.

Next, we check the thermal stability of this structure by performing AIMD simulations at 500 and 800 K, respectively. These calculations simulate the thermal motion of atoms within 10 picosecond (ps) with a time step of 1 femtosecond (fs). A $3 \times 3 \times 1$ supercell of the cco-Si₄₈ primitive cell is used to avoid the fake stability caused by the unrealistic interactions between an atom and its periodic images. As shown in Fig. 2(c) and Fig. S2 in the ESI,[†] the total potential energies change slightly around constants in both simulations, and the geometry of cco-Si₄₈ at the end of both simulations remains almost intact without broken chemical bonds, indicating that cco-Si₄₈ is thermally stable at high temperatures up to 800 K.

Then, we examine the mechanical stability of cco-Si₄₈ by calculating its elastic constants. The nonzero independent elastic constants of this orthorhombic system are calculated to be $C_{11} = 172.56$ GPa, $C_{22} = 181.82$ GPa, $C_{33} = 137.23$ GPa, $C_{12} = 37.57$ GPa, $C_{13} = 33.34$ GPa, $C_{23} = 41.04$ GPa, $C_{44} = 41.81$ GPa, $C_{55} = 36.33$ GPa, and $C_{66} = 42.21$ GPa. These elastic constants fully satisfy the Born–Huang criteria³⁹ for an orthorhombic system,⁴⁰ which require $C_{ii} > 0$ ($i \in [1, 6] \cap \mathbb{Z}$), $C_{ii} + C_{jj} - 2C_{ij} > 0$ ($i < j$; $i, j \in [1, 3] \cap \mathbb{Z}$), and $C_{11} + C_{22} + C_{33} + 2(C_{12} + C_{13} + C_{23}) > 0$. Thus, cco-Si₄₈ is mechanically stable.

We also calculate the Young's modulus E of cco-Si₄₈ with these elastic constants based on the following equation:⁴¹

$$E^{-1} = s_{11}l_1^4 + s_{22}l_2^4 + s_{33}l_3^4 + 2s_{12}l_1^2l_2^2 + 2s_{13}l_1^2l_3^2 + 2s_{23}l_2^2l_3^2 + s_{44}l_2^2l_3^2 + s_{55}l_1^2l_3^2 + s_{66}l_1^2l_2^2, \quad (3)$$

where $(s_{ij})_{6 \times 6} = (C_{ij})_{6 \times 6}^{-1}$ is the elastic compliance matrix and $l_1/l_2/l_3$ is the cosine of the angle between an arbitrary direction and the positive direction of $x/y/z$ -axis. The resulting orientation-dependent Young's moduli in the first quadrant ($l_1, l_2, l_3 \geq 0$) are shown in Fig. 3. The Young's moduli along the three axial directions are 159.97, 164.91 and 124.22 GPa, respectively, which are all local maxima. Such anisotropy can be expected because the Young's modulus is generally determined by the weakest part in the structure, which is along the direction where the penta-silicene nanoribbons are connected

in the head-on pattern, since there are fewer Si–Si bonds while the minimum Young's modulus is found to be 99.93 GPa near the diagonal direction.

3.2. Electronic structure

Next, we calculate the electronic band structure of cco-Si₄₈ at the HSE06 level. As shown in Fig. 4(a), cco-Si₄₈ is semiconducting with a direct bandgap of 1.46 eV at the high symmetry point Y. For comparison, the band structure at the PBE level is also calculated and plotted in Fig. 4(a), showing a similar band dispersion with a smaller bandgap of 0.88 eV, because the PBE functional systematically underestimates the bandgap.⁴² Unlike the valence band maximum (VBM) in the band structure, the conductive band minimum (CBM) at the high symmetry point Y (denoted as CBM₁) almost degenerates in energy with the other two electronic states on the high symmetry paths $Y \rightarrow X_1$ and $X \rightarrow \Gamma$, which are denoted as CBM₂ and CBM₃, respectively. The energy difference between CBM₂/CBM₃ and CBM₁ is only 0.01/0.02 eV, which can be covered by the thermal fluctuation at room temperature. Density of states (DOS) and projected DOS (PDOS) on different Si atoms are plotted in Fig. 4(a), which shows that the electronic states near the VBM and CBM are both nearly equally contributed by the Si atoms on the three nonequivalent Wyckoff positions. In addition, we analyze the band and k -point decomposed charge densities. As shown in Fig. 4(b), one can see that the electronic states near the VBM are indeed contributed by all the Si atoms, while, the electronic states near the CBM₁ are mostly localized around the Si atoms at the $16g_1$ and $16g_3$ positions, and the electronic states near the CBM₂ and CBM₃ are nearly localized around the Si–Si bonds between the atoms at the $16g_1$ and $16g_2$ positions. The overall contribution from the CBM₁, CBM₂ and CBM₃ adds up to the near-equal contribution from the different Si atoms to the PDOS.

Since silicon semiconductors with direct bandgaps usually show strong optical absorption, we calculate the linear optical responses of cco-Si₄₈ and find that it would possess a predominant power conversion efficiency as a solar cell due to its strong optical absorption comparable to that of diamond silicon^{43,44} and its moderate direct bandgap, as is the case with Pd₂Se₃⁴⁵ and polymer–fullerene solar cells.⁴⁶ More details can be found in Text S2 and Fig. S3 in the ESI.[†] It is also worth mentioning that the accidental degeneracy at the band edge is among the common mechanisms for strong thermoelectric response since it contributes to a large DOS. However, the carrier transport properties of such materials are rarely investigated because the commonly used Bardeen–Shockley equation⁴⁷ (also known as the deformation potential theory) for obtaining the carrier mobility is not well defined when intervalley scattering processes related to degenerated electronic states are involved. Instead, we study these properties by directly solving the BTE for electrons at the e–ph level, as discussed in the following section.

3.3. Electron transport properties

We calculate the electron transport properties of cco-Si₄₈ by using the Perturbo code³¹ as interfaced with QE.¹⁹

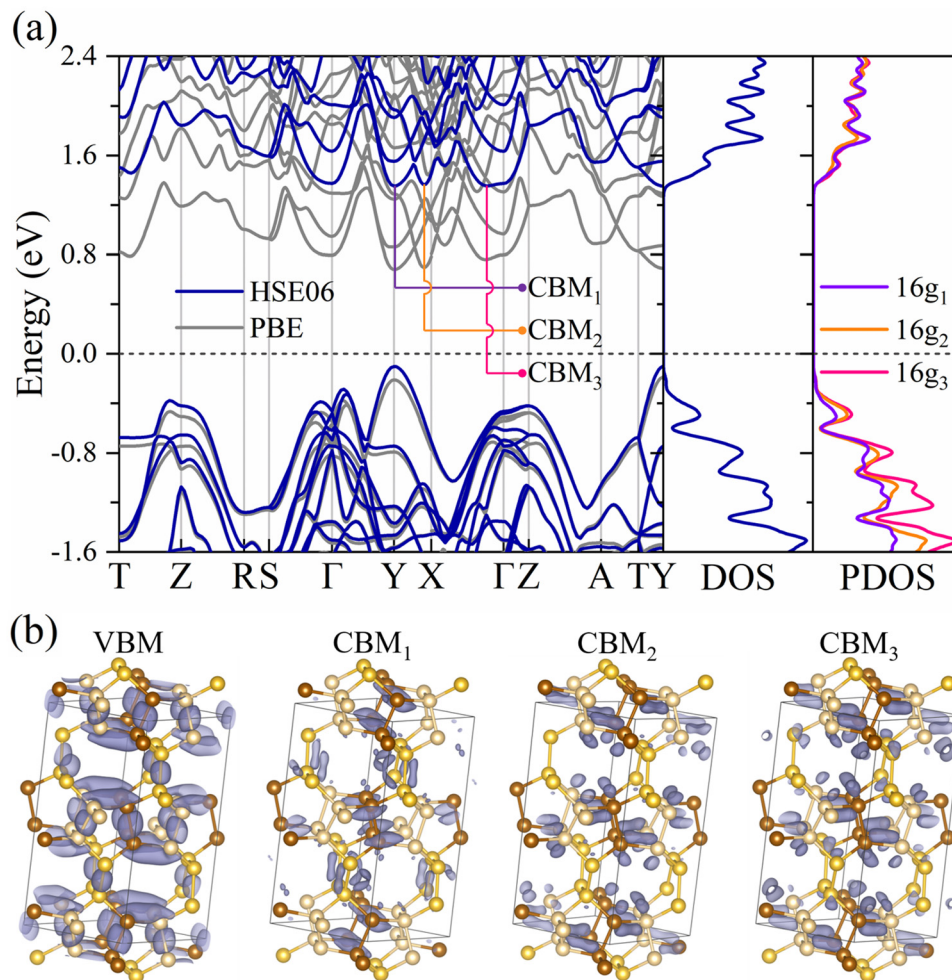


Fig. 4 (a) Electronic band structure, DOS and PDOS of cco-Si₄₈. (b) Decomposed charge density distribution at the VBM and the degenerated CBMs (isosurface value = 0.0018 Å⁻³).

The electronic structure obtained by QE at the PBE level is comparable with that obtained from our VASP calculations, as confirmed by the electronic band structures from both approaches and illustrated in Fig. S4 in the ESI.† The electron

and hole transport properties at the e-ph level are calculated in two separate calculations involving the Wannierized electronic states in the vicinity (± 0.3 eV) of the VBM and CBM, respectively. The deeper energy states are neglected in the e-ph

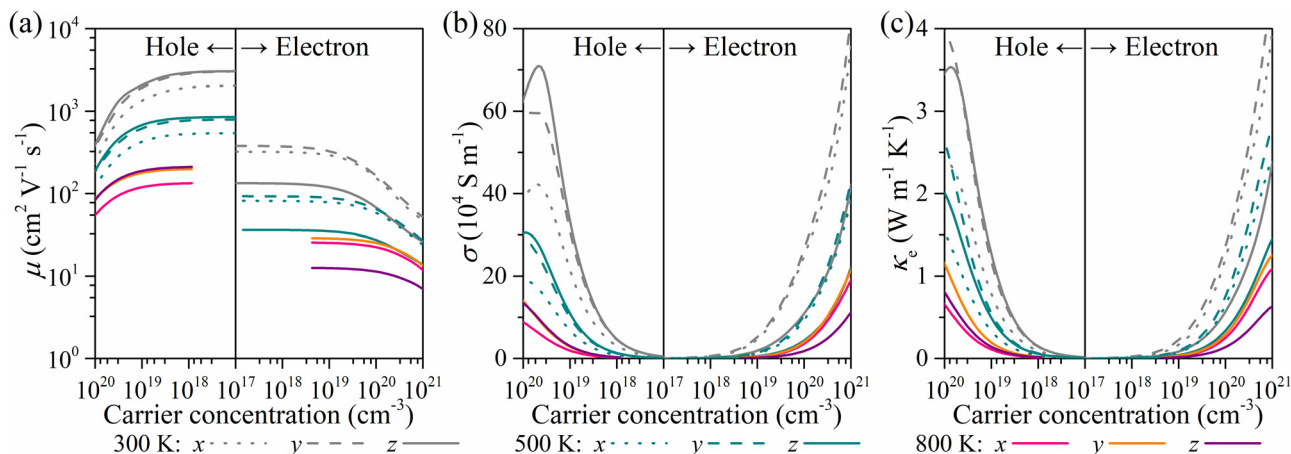


Fig. 5 Variation of (a) carrier mobility μ , (b) electric conductivity σ , and (c) electronic thermal conductivity κ_e of cco-Si₄₈ with carrier concentration.

Table 1 Converged electron and hole mobilities (in $10^3 \text{ cm}^2 \text{ V}^{-1} \text{ s}^{-1}$) of cco-Si₄₈ at low carrier concentrations n_e and n_h (in 10^{17} cm^{-3})

T (K)	n_e	$\mu_{e,x}$	$\mu_{e,y}$	$\mu_{e,z}$	n_h	$\mu_{h,x}$	$\mu_{h,y}$	$\mu_{h,z}$
300	1.02	0.323	0.380	0.134	1.00	2.04	3.03	3.05
500	1.43	0.082	0.093	0.036	1.01	0.543	0.794	0.853
800	43.13	0.026	0.029	0.013	8.63	0.134	0.199	0.211

interactions because they are either nearly empty or almost fully occupied by electrons according to the Fermi–Dirac distribution, and they have little contribution to the scattering processes. The results are plotted in Fig. 5 as a function of the carrier concentration. For comparison, the electron transport properties of diamond silicon are calculated at the same level and summarized in Fig. S5 in the ESI.† As shown in Fig. 5(a), the electron mobilities (μ_e) along the x and y directions are comparable and are about twice as large as that along the z direction, while the hole mobilities (μ_h) along the y and z directions are comparable and are larger than that along the x direction by 50%. At a given temperature, the values of μ_e and μ_h along each axial direction converge to certain levels at low carrier concentrations, as summarized in Table 1. The hole mobility of cco-Si₄₈ reaches up to $3.05 \times 10^3 \text{ cm}^2 \text{ V}^{-1} \text{ s}^{-1}$ at 300 K, while the electron mobility of cco-Si₄₈ is about an order of magnitude lower due to the complex scattering processes

among the degenerated CBM₁, CBM₂, and CBM₃ states. In contrast, the peak electron and hole mobilities of diamond silicon are ~ 2000 and $\sim 200 \text{ cm}^2 \text{ V}^{-1} \text{ s}^{-1}$, respectively. The electron and hole mobilities decrease with the increasing carrier concentration, since the properties of the carriers on the relatively deeper energy states deviate from those at the band edge. We note that the results in Table 1 diverge from the $\mu \propto T^{-3/2}$ trend predicted by the Bardeen–Shockley equation for bulk materials,⁴⁷ which can be attributed to the deviation of the electronic band structure from the ideal parabolic dispersion. The corresponding electric conductivities are plotted in Fig. 5(b), and are connected to the carrier mobility values based on the equations $\sigma_e = n_e e \mu_e$ and $\sigma_h = n_h e \mu_h$, where σ_e (σ_h) is the electric conductivity from electrons (holes), n_e (n_h) is the electron (hole) concentration, and e is the elementary charge.

The electronic thermal conductivity κ_e of cco-Si₄₈ is also calculated at the e–ph level, and the results at different temperatures are plotted in Fig. 5(c). While the famous Wiedemann–Franz law states that κ_e is proportional to the electric conductivity σ , leading to a constant scale factor termed Lorenz number $L = \kappa_e / \sigma T = 1.5 \times 10^{-8} \text{ W } \Omega \text{ K}^{-2}$.⁴⁸ However, the $\kappa_e / \sigma T$ value at the e–ph level is dependent on the temperature, carrier, and the lattice structure,³³ as shown in Fig. S6 in the ESI.† In particular, the $\kappa_e / \sigma T$ value at a hole concentration of 10^{18} cm^{-3} decreases to $\sim 6 \times 10^{-9} \text{ W } \Omega \text{ K}^{-2}$ at 800 K, and is 60% lower than that estimated by using the Wiedemann–Franz law.

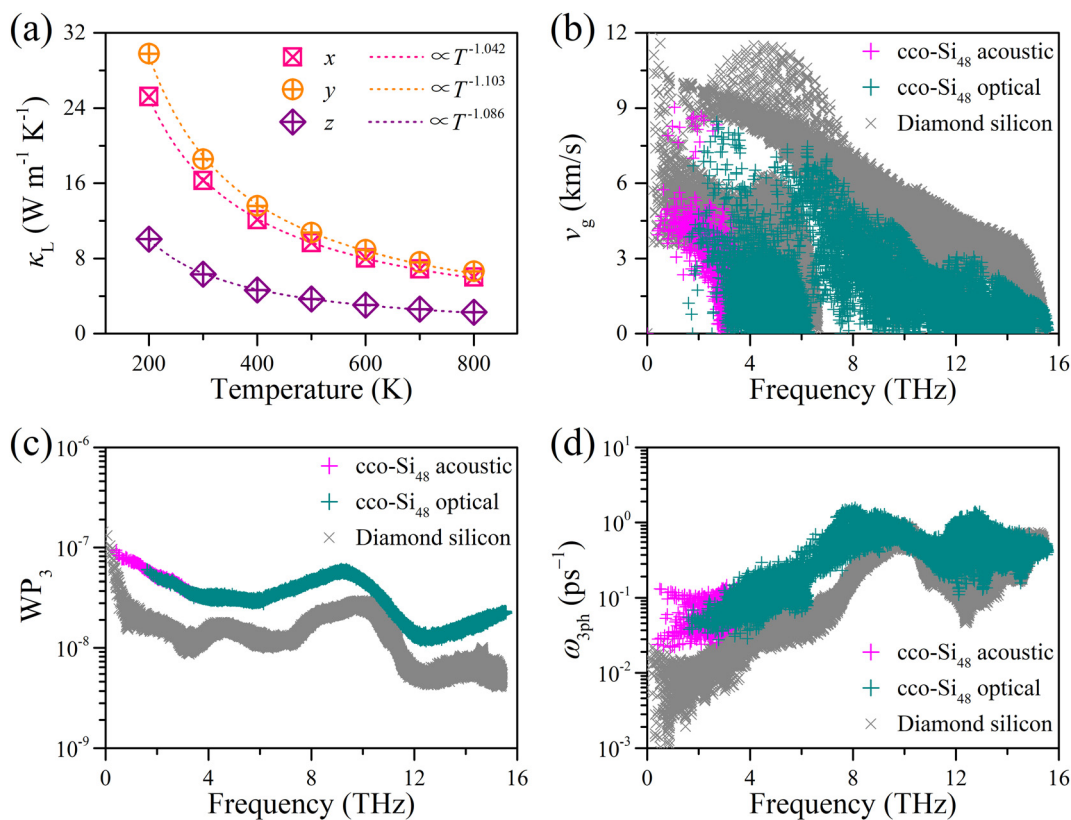


Fig. 6 (a) Lattice thermal conductivities, (b) group velocities, (c) weighted three-phonon phase space, and (d) three-phonon scattering rates of cco-Si₄₈ and diamond silicon.

Table 2 Lattice thermal conductivities $\kappa_{L,x}$, $\kappa_{L,y}$, and $\kappa_{L,z}$ of cco-Si₄₈ and some previously reported silicon allotropes (in W m⁻¹ K⁻¹) at 300 K

Materials	$\kappa_{L,x}$	$\kappa_{L,y}$	$\kappa_{L,z}$
cco-Si ₄₈ (this work)	16.31	18.57	6.33
Diamond silicon ⁴⁹	146	146	146
BC8-Si ⁵⁰	26.96	26.96	26.96
R8-Si ⁵¹	16.83	16.83	8.95
Pentagonal Si ⁵²	59.9	60.1	60.4

3.4. Lattice thermal conductivity

In addition to the electronic thermal conductivity, we calculate the lattice thermal conductivity κ_L of cco-Si₄₈ with the ShengBTE code³⁵ to obtain an overview on its thermal transport properties. The 3rd-order IFCs as the input to the code are obtained using the HiPhive package.³⁸ The calculated κ_L values of cco-Si₄₈ at different temperatures are plotted in Fig. 6(a), which shows that the κ_L values along the *x* and *y* directions are comparable and are over 150% larger than that along the *z* direction. Such anisotropy in the lattice thermal conductivity coincides with that in its mechanical properties, where the Young's modulus along the *z* direction is also lower than those along the *x* and *y* directions, respectively. The κ_L values along the three axial directions all decay with the temperature in a T^{-1} relationship and the corresponding values at 300 K are 16.31, 18.57, and 6.33 W m⁻¹ K⁻¹ along the *x*, *y*, and *z* directions, respectively. For comparison, the κ_L values of other silicon allotropes are summarized in Table 2. The κ_L values of cco-Si₄₈ are an order of magnitude lower than those of diamond silicon (146 W m⁻¹ K⁻¹)⁴⁹ and are lower than those of some recently reported 3D silicon allotropes.^{50–52}

The decrease in the κ_L of cco-Si₄₈ with respect to that of the diamond silicon can be attributed to its weakened harmonicity and enhanced anharmonicity. The harmonicity can be represented by the group velocity (v_g) and the weighted three-phonon phase space (WP₃), which are obtained directly from the phonon dispersion. The calculated results are presented in

Fig. 6(b) and (c). One can see that both the v_g values of the acoustic and optical phonon modes in cco-Si₄₈ are lower than those in diamond silicon, indicating that the phonon transport is damped in the cco-Si₄₈ lattice, which is due to the complex phonon dispersion resulting from its complex primitive cell. The WP₃ of cco-Si₄₈ is much larger than that of diamond silicon, indicating more complex scattering channels. The two parameters indicate that the harmonicity of cco-Si₄₈ is weaker than that in diamond silicon. Meanwhile, the anharmonicity of cco-Si₄₈ is revealed by its three-phonon scattering rate (ω_{3ph}) in Fig. 6(d) and its Grüneisen parameter (γ) in Fig. S7 in the ESI.† The ω_{3ph} value of cco-Si₄₈ is about an order of magnitude larger than that of diamond silicon in the low frequency region (<3 THz), indicating a strong anharmonicity in the cco-Si₄₈ lattice, while more negative values are found in the frequency-dependent Grüneisen parameters of cco-Si₄₈, leading to a total Grüneisen parameter of -0.71 at 300 K, which is twice as large as that of diamond silicon (0.35 at 300 K) in terms of absolute value. The large absolute value of the total Grüneisen parameter γ of cco-Si₄₈ is consistent with its low κ_L values according to the empirical $\kappa_L \propto \gamma^{-2}$ relationship.⁵³

3.5. Thermoelectricity

Based on the electron and phonon transport properties of cco-Si₄₈, we examine its potential as a thermoelectric material by evaluating its $ZT = S^2\sigma T/(\kappa_e + \kappa_L)$ at various temperatures and carrier concentrations. The Seebeck coefficient S is calculated by using the Perturbo code at the e-ph level. As shown in Fig. 7(a), in spite of the anisotropic nature of cco-Si₄₈, its Seebeck coefficients along the different axial directions are almost the same. The Seebeck coefficients of the n-type cco-Si₄₈ are larger than those of the p-type one due to the high DOS caused by the accidental degeneration near the VBM. The calculated ZT values are plotted in Fig. 7(b). Unlike the predominant n-type thermoelectricity in diamond silicon and many other silicon allotropes,^{12–14} the ZT values of the p-type

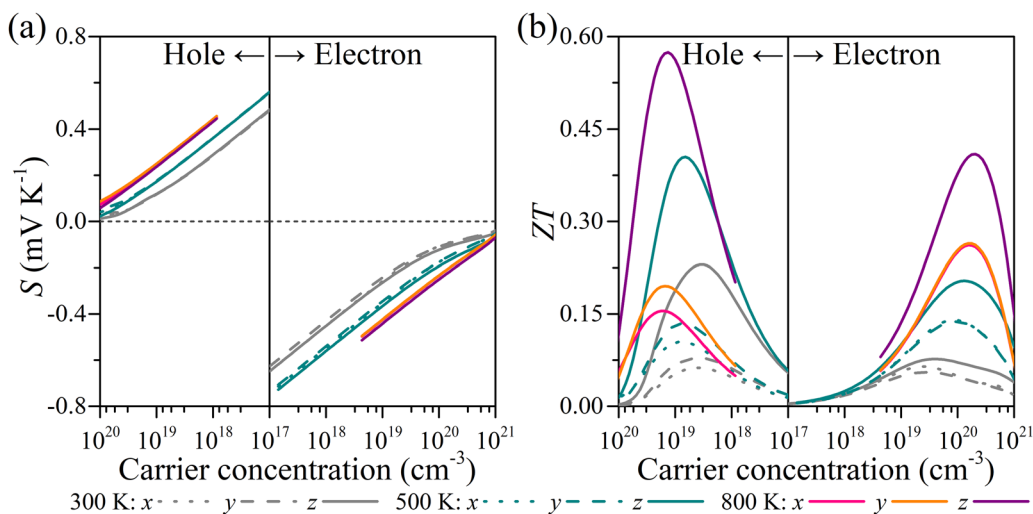


Fig. 7 (a) Seebeck coefficient and (b) ZT of cco-Si₄₈.

cco-Si₄₈ are larger than those of the n-type cco-Si₄₈ due to its high hole mobility in the order of magnitude of $10^3 \text{ cm}^2 \text{ V}^{-1} \text{ s}^{-1}$. The optimal ZT values for p-type and n-type cco-Si₄₈ are found to be 0.57 ($n_h = 1.34 \times 10^{19} \text{ cm}^{-3}$) and 0.41 ($n_e = 2.06 \times 10^{20} \text{ cm}^{-3}$), respectively, at 800 K and are both along the z direction. These values are about 9 and 3 times larger than those of diamond silicon, respectively, as shown in Fig. S8 in the ESI.† Considering the fact that nanostructures in diamond silicon lead to significantly improved thermoelectric properties,¹² higher ZT values can be expected in nanostructured cco-Si₄₈. It is also worth mentioning that the carrier concentrations corresponding to the optimal ZT values increase with temperature, which is different from the common results from many previous reports.^{54–56} This is because the carrier mobility at the e–ph level is a monotonically decreasing function of the carrier concentration rather than a constant provided by the Bardeen–Shockley equation. The decline in carrier mobilities at high carrier concentrations indicates that the transport of an average carrier is hindered, so that the peak value of ZT appears at even higher carrier concentrations where the hindered transport of an averaged carrier is compensated by the amount of carriers. In contrast, the constant carrier mobilities from the Bardeen–Shockley equation would underestimate the optimal carrier concentrations.

4. Conclusions

In summary, based on first principles calculations, we propose a new 3D silicon allotrope termed cco-Si₄₈, which is the first silicon allotrope composed of the experimentally synthesized PSNRs and is thermally, dynamically, and mechanically stable. Different from silicene nanoribbon-based 3D silicon that is topologically semi-metallic,⁵⁷ cco-Si₄₈ is a direct bandgap semiconductor with a gap of 1.46 eV and a high hole mobility up to $3.05 \times 10^3 \text{ cm}^2 \text{ V}^{-1} \text{ s}^{-1}$ at room temperature. The lattice thermal conductivity of cco-Si₄₈ is $6.33 \text{ W m}^{-1} \text{ K}^{-1}$ at 300 K, and is about an order of magnitude lower than that of diamond silicon due to its weak harmonicity and strong anharmonicity. The optimal ZT values of the p- and n-type cco-Si₄₈ reach 0.57 and 0.41 at 800 K, respectively, making it a potential p-type thermoelectric material, which is superior among silicon allotropes. We also show that the e–ph interactions are important for a more accurate relationship between the optimal ZT values and the carrier concentrations. We hope that this study could stimulate experimental efforts in synthesizing PSNR-based materials and other pentagon-based materials for the applications in the field of energy conversion.

Conflicts of interest

There are no conflicts to declare.

Acknowledgements

This work is partially supported by grants from the National Natural Science Foundation of China (Grant No. NSFC-11974028

and NSFC-12274007) and the National Key Research and Development Program of the Ministry of Science and Technology of China (2017YFA0205003). It is also supported by the High-Performance Computing Platform of Peking University, China.

References

- 1 S. Zhang, J. Zhou, Q. Wang, X. Chen, Y. Kawazoe and P. Jena, Penta-graphene: A new carbon allotrope, *Proc. Natl. Acad. Sci. U. S. A.*, 2015, **112**, 2372–2377.
- 2 M. A. Nazir, A. Hassan, Y. H. Shen and Q. Wang, Research progress on penta-graphene and its related materials: Properties and applications, *Nano Today*, 2022, **44**, 101501.
- 3 J. I. Cerdá, J. Slawinska, G. Le Lay, A. C. Marele, J. M. Gomez-Rodriguez and M. E. Davila, Unveiling the pentagonal nature of perfectly aligned single- and double-strand Si nano-ribbons on Ag(110), *Nat. Commun.*, 2016, **7**, 13076.
- 4 G. Prevot, C. Hogan, T. Leoni, R. Bernard, E. Moyen and L. Masson, Si nanoribbons on Ag(110) studied by grazing-incidence X-ray diffraction, scanning tunneling microscopy, and density-functional theory: Evidence of a pentamer chain structure, *Phys. Rev. Lett.*, 2016, **117**, 276102.
- 5 S. Sheng, R. Ma, J. B. Wu, W. Li, L. Kong, X. Cong, D. Cao, W. Hu, J. Gou, J. W. Luo, P. Cheng, P. H. Tan, Y. Jiang, L. Chen and K. Wu, The pentagonal nature of self-assembled silicon chains and magic clusters on Ag(110), *Nano Lett.*, 2018, **18**, 2937–2942.
- 6 S. Yue, H. Zhou, Y. Feng, Y. Wang, Z. Sun, D. Geng, M. Arita, S. Kumar, K. Shimada, P. Cheng, L. Chen, Y. Yao, S. Meng, K. Wu and B. Feng, Observation of one-dimensional Dirac Fermions in silicon nanoribbons, *Nano Lett.*, 2022, **22**, 695–701.
- 7 Y. Guo, C. Zhang, J. Zhou, Q. Wang and P. Jena, Lattice dynamic and instability in pentasilicene: A light single-element ferroelectric material with high Curie temperature, *Phys. Rev. Appl.*, 2019, **11**, 064063.
- 8 L. Zhan, Y. Fang, R. Zhang, X. Lu, T. Y. Lu, X. Cao, Z. Zhu and S. Wu, Quantum spin Hall effect in tilted penta silicene and its isoelectronic substitutions, *Phys. Chem. Chem. Phys.*, 2022, **24**, 15201–15207.
- 9 Z. P. Chen, W. C. Ren, L. B. Gao, B. L. Liu, S. F. Pei and H. M. Cheng, Three-dimensional flexible and conductive interconnected graphene networks grown by chemical vapour deposition, *Nat. Mater.*, 2011, **10**, 424–428.
- 10 N. V. Krainyukova and E. N. Zubarev, Carbon honeycomb high capacity storage for gaseous and liquid species, *Phys. Rev. Lett.*, 2016, **116**, 055501.
- 11 L. Weber and E. Gmelin, Transport-properties of silicon, *Appl. Phys. A: Mater. Sci. Process.*, 1991, **53**, 136–140.
- 12 S. K. Bux, R. G. Blair, P. K. Gogna, H. Lee, G. Chen, M. S. Dresselhaus, R. B. Kaner and J.-P. Fleurial, Nanostructured bulk silicon as an effective thermoelectric material, *Adv. Funct. Mater.*, 2009, **19**, 2445–2452.
- 13 A. I. Hochbaum, R. Chen, R. D. Delgado, W. Liang, E. C. Garnett, M. Najarian, A. Majumdar and P. Yang,

- Enhanced thermoelectric performance of rough silicon nanowires, *Nature*, 2008, **451**, 163–167.
- 14 H. Zhang, H. Liu, K. Wei, O. O. Kurakevych, Y. Le Godec, Z. Liu, J. Martin, M. Guerrette, G. S. Nolas and T. A. Strobel, BC8 Silicon (Si-III) is a narrow-gap semiconductor, *Phys. Rev. Lett.*, 2017, **118**, 146601.
 - 15 G. S. Nolas, M. Beekman, J. Gryko, G. A. Lamberton, T. M. Tritt and P. F. McMillan, Thermal conductivity of elemental crystalline silicon clathrate Si₁₃₆, *Appl. Phys. Lett.*, 2003, **82**, 910–912.
 - 16 F. Q. Wang, M. Hu and Q. Wang, Ultrahigh thermal conductivity of carbon allotropes with correlations with the scaled Pugh ratio, *J. Mater. Chem. A*, 2019, **7**, 6259–6266.
 - 17 G. Kresse and J. Furthmuller, Efficient iterative schemes for ab initio total-energy calculations using a plane-wave basis set, *Phys. Rev. B: Condens. Matter Mater. Phys.*, 1996, **54**, 11169–11186.
 - 18 G. Kresse and J. Furthmuller, Efficiency of ab-initio total energy calculations for metals and semiconductors using a plane-wave basis set, *Comput. Mater. Sci.*, 1996, **6**, 15–50.
 - 19 P. Giannozzi, S. Baroni, N. Bonini, M. Calandra, R. Car, C. Cavazzoni, D. Ceresoli, G. L. Chiarotti, M. Cococcioni, I. Dabo, A. Dal Corso, S. de Gironcoli, S. Fabris, G. Fratesi, R. Gebauer, U. Gerstmann, C. Gougoussis, A. Kokalj, M. Lazzeri, L. Martin-Samos, N. Marzari, F. Mauri, R. Mazzarello, S. Paolini, A. Pasquarello, L. Paulatto, C. Sbraccia, S. Scandolo, G. Sclauzero, A. P. Seitsonen, A. Smogunov, P. Umari and R. M. Wentzcovitch, QUANTUM ESPRESSO: A modular and open-source software project for quantum simulations of materials, *J. Phys.: Condens. Matter*, 2009, **21**, 395502.
 - 20 P. Giannozzi, O. Andreussi, T. Brumme, O. Bunau, M. B. Nardelli, M. Calandra, R. Car, C. Cavazzoni, D. Ceresoli, M. Cococcioni, N. Colonna, I. Carnimeo, A. Dal Corso, S. de Gironcoli, P. Delugas, R. A. DiStasio, A. Ferretti, A. Floris, G. Fratesi, G. Fugallo, R. Gebauer, U. Gerstmann, F. Giustino, T. Gorni, J. Jia, M. Kawamura, H. Y. Ko, A. Kokalj, E. Kucukbenli, M. Lazzeri, M. Marsili, N. Marzari, F. Mauri, N. L. Nguyen, H. V. Nguyen, A. Otero-de-la-Roza, L. Paulatto, S. Ponce, D. Rocca, R. Sabatini, B. Santra, M. Schlipf, A. P. Seitsonen, A. Smogunov, I. Timrov, T. Thonhauser, P. Umari, N. Vast, X. Wu and S. Baroni, Advanced capabilities for materials modelling with QUANTUM ESPRESSO, *J. Phys.: Condens. Matter*, 2017, **29**, 465901.
 - 21 P. E. Blöchl, Projector augmented-wave method, *Phys. Rev. B: Condens. Matter Mater. Phys.*, 1994, **50**, 17953–17979.
 - 22 J. P. Perdew, K. Burke and M. Ernzerhof, Generalized gradient approximation made simple, *Phys. Rev. Lett.*, 1996, **77**, 3865–3868.
 - 23 M. P. Teter, M. C. Payne and D. C. Allan, Solution of Schrodinger-equation for large systems, *Phys. Rev. B: Condens. Matter Mater. Phys.*, 1989, **40**, 12255–12263.
 - 24 J. Heyd, G. E. Scuseria and M. Ernzerhof, Hybrid functionals based on a screened Coulomb potential, *J. Chem. Phys.*, 2003, **118**, 8207–8215.
 - 25 J. Heyd, G. E. Scuseria and M. Ernzerhof, Erratum: Hybrid functionals based on a screened Coulomb potential, *J. Chem. Phys.*, 2006, **124**, 219906.
 - 26 S. Nosé, A unified formulation of the constant temperature molecular dynamics methods, *J. Chem. Phys.*, 1984, **81**, 511–519.
 - 27 M. J. van Setten, M. Giantomassi, E. Bousquet, M. J. Verstraete, D. R. Hamann, X. Gonze and G. M. Rignanese, The PSEUDO-DOJO: Training and grading a 85 element optimized norm-conserving pseudopotential table, *Comput. Phys. Commun.*, 2018, **226**, 39–54.
 - 28 N. Marzari and D. Vanderbilt, Maximally localized generalized Wannier functions for composite energy bands, *Phys. Rev. B: Condens. Matter Mater. Phys.*, 1997, **56**, 12847–12865.
 - 29 I. Souza, N. Marzari and D. Vanderbilt, Maximally localized Wannier functions for entangled energy bands, *Phys. Rev. B: Condens. Matter Mater. Phys.*, 2002, **65**, 035109.
 - 30 G. Pizzi, V. Vitale, R. Arita, S. Blugel, F. Freimuth, G. Geranton, M. Gibertini, D. Gresch, C. Johnson, T. Koretsune, J. Ibanez-Azpiroz, H. Lee, J. M. Lihm, D. Marchand, A. Marrazzo, Y. Mokrousov, J. I. Mustafa, Y. Nohara, Y. Nomura, L. Paulatto, S. Ponce, T. Ponweiser, J. F. Qiao, F. Thole, S. S. Tsirkin, M. Wierzbowska, N. Marzari, D. Vanderbilt, I. Souza, A. A. Mostofi and J. R. Yates, Wannier90 as a community code: New features and applications, *J. Phys.: Condens. Matter*, 2020, **32**, 165902.
 - 31 J.-J. Zhou, J. Park, I. T. Lu, I. Maliyov, X. Tong and M. Bernardi, Perturbo: A software package for ab initio electron–phonon interactions, charge transport and ultrafast dynamics, *Comput. Phys. Commun.*, 2021, **264**, 107970.
 - 32 W. Li, Electrical transport limited by electron-phonon coupling from Boltzmann transport equation: An ab initio study of Si, Al, and MoS₂, *Phys. Rev. B: Condens. Matter Mater. Phys.*, 2015, **92**, 075405.
 - 33 M. Fiorentini and N. Bonini, Thermoelectric coefficients of n-doped silicon from first principles via the solution of the Boltzmann transport equation, *Phys. Rev. B: Condens. Matter Mater. Phys.*, 2016, **94**, 085204.
 - 34 M. Omini and A. Sparavigna, An iterative approach to the phonon Boltzmann-equation in the theory of thermal-conductivity, *Phys. Rev. B: Condens. Matter Mater. Phys.*, 1995, **212**, 101–112.
 - 35 W. Li, J. Carrete, N. A. Katcho and N. Mingo, ShengBTE: A solver of the Boltzmann transport equation for phonons, *Comput. Phys. Commun.*, 2014, **185**, 1747–1758.
 - 36 A. Togo, F. Oba and I. Tanaka, First-principles calculations of the ferroelastic transition between rutile-type and CaCl₂-type SiO₂ at high pressures, *Phys. Rev. B: Condens. Matter Mater. Phys.*, 2008, **78**, 134106.
 - 37 A. Togo and I. Tanaka, First principles phonon calculations in materials science, *Scripta Mater.*, 2015, **108**, 1–5.
 - 38 F. Eriksson, E. Fransson and P. Erhart, The Hiphive package for the extraction of high-order force constants by machine learning, *Adv. Theory Simul.*, 2019, **2**, 1800184.
 - 39 M. Born and K. Huang, *Dynamical theory of crystal lattices*, Clarendon Press, 1954.
 - 40 D. Y. Ni, Y. H. Shen, W. Sun and Q. Wang, Design of 3D topological nodal-net porous carbon for sodium-ion battery anodes, *J. Mater. Chem. A*, 2022, **10**, 7754–7763.

- 41 Z. Y. Wei, K. M. Hu, B. S. Sa and B. Wu, Pressure-induced structure, electronic, thermodynamic and mechanical properties of Ti_2AlNb orthorhombic phase by first-principles calculations, *Rare Met.*, 2021, **40**, 2964–2974.
- 42 J. Paier, M. Marsman, K. Hummer, G. Kresse, I. C. Gerber and J. G. Angyan, Screened hybrid density functionals applied to solids, *J. Chem. Phys.*, 2006, **124**, 154709.
- 43 R. Braunstein, A. R. Moore and F. Herman, Intrinsic optical absorption in germanium-silicon alloys, *Phys. Rev.*, 1958, **109**, 695–710.
- 44 J. Noffsinger, E. Kioupakis, C. G. Van de Walle, S. G. Louie and M. L. Cohen, Phonon-assisted optical absorption in silicon from first principles, *Phys. Rev. Lett.*, 2012, **108**, 167402.
- 45 X. Y. Li, S. H. Zhang, Y. G. Guo, F. Q. Wang and Q. Wang, Physical properties and photovoltaic application of semi-conducting Pd_2Se_3 monolayer, *Nanomaterials*, 2018, **8**, 832.
- 46 M. C. Scharber, D. Mühlbacher, M. Koppe, P. Denk, C. Waldauf, A. J. Heeger and C. J. Brabec, Design rules for donors in bulk-heterojunction solar cells—Towards 10% energy-conversion efficiency, *Adv. Mater.*, 2006, **18**, 789–794.
- 47 J. Bardeen and W. Shockley, Deformation Potentials and Mobilities in Non-polar Crystals, *Phys. Rev.*, 1950, **80**, 72–80.
- 48 H. S. Kim, Z. M. Gibbs, Y. L. Tang, H. Wang and G. J. Snyder, Characterization of Lorenz number with Seebeck coefficient measurement, *APL Mater.*, 2015, **3**, 041506.
- 49 B. Liao, B. Qiu, J. Zhou, S. Huberman, K. Esfarjani and G. Chen, Significant reduction of lattice thermal conductivity by the electron-phonon interaction in silicon with high carrier concentrations: A first-principles study, *Phys. Rev. Lett.*, 2015, **114**, 115901.
- 50 J. Liu, T. A. Strobel, H. Zhang, D. Abernathy, C. Li and J. Hong, Significant phase-space-driven thermal transport suppression in BC8 silicon, *Mater. Today Phys.*, 2021, **21**, 100566.
- 51 Y. Rao, C. Y. Zhao and S. Ju, High thermoelectric performance in metastable phase of silicon: A first-principles study, *Appl. Phys. Lett.*, 2022, **120**, 163901.
- 52 P. H. Du and J. Zhou, Thermal property and lattice thermal conductivity of three-dimensional pentagonal silicon, *Phys. Rev. B: Condens. Matter Mater. Phys.*, 2021, **618**, 413178.
- 53 E. S. Toberer, A. Zevkink and G. J. Snyder, Phonon engineering through crystal chemistry, *J. Mater. Chem.*, 2011, **21**, 15843–15852.
- 54 F. Q. Wang, Y. G. Guo, Q. Wang, Y. Kawazoe and P. Jena, Exceptional thermoelectric properties of layered $GeAs_2$, *Chem. Mater.*, 2017, **29**, 9300–9307.
- 55 Y. Chen, Y. Shen, X. Li, J. Sun and Q. Wang, β - $CsCu_5Se_3$: A promising thermoelectric material going beyond photovoltaic application, *Adv. Theory Simul.*, 2020, **3**, 2000169.
- 56 Y. Y. Chen, J. Sun, W. Kang and Q. Wang, Phonon transport and thermoelectric properties of imidazole-graphyne, *Materials*, 2021, **14**, 5604.
- 57 Y. Qie, J. Y. Liu, X. Y. Li, S. Wang, Q. Sun and P. Jena, Interpenetrating silicene networks: A topological nodal-line semimetal with potential as an anode material for sodium ion batteries, *Phys. Rev. Mater.*, 2018, **2**, 084201.